Article

INTERNATIONAL JOURNAL OF DAMAGE MECHANICS

International Journal of Damage Mechanics
2018, Vol. 27(3) 439–450

DOI: 10.1177/1056789516683539
journals.sagepub.com/home/ijd

SAGE

Crushing of circular steel tubes filled with nanoporous-materials-functionalized liquid

Yueting Sun[1,2], Yibing Li[2], Cang Zhao[1], Meng Wang[1], Weiyi Lu[1,3] and Yu Qiao[1,4]

Abstract

The crush behaviors of steel tubes filled with nanoporous-materials-functionalized liquids are experimentally investigated under quasi-static and dynamic conditions. Results show that the nanoporous-materials-functionalized liquid can enhance the load-carrying and the energy absorption capacities of thin-walled tubes, as the buckling mode is affected. The effective buckling stress increases with the infiltration pressure, and the overall compressibility is highly dependent on the nanopore volume. A general rule of designing nanoporous-materials-functionalized liquid-filled tubes is proposed. The interaction between the tube wall and the nanoporous-materials-functionalized liquid is analyzed.

Keywords

Thin-walled tube, crush behavior, nanoporous material, energy absorption, dynamic behavior

Introduction

Development of energy absorption materials and structures (EAMS) has attracted increasing attention for many decades (Lu and Yu, 2003). By using a relatively "soft" EAMS, in a blunt impact, the velocity of impactor can be reduced before it reaches the target, so that the generated stress waves are less intense; in a blast attack, the EAMS dissipate the energy carried by stress waves, so that the transmitted wave pressure is decreased. Such protective/damping mechanisms are widely utilized for vehicle crashworthiness (Zhang et al., 2012), human body protection (Majumdar et al., 2013), seismic resistant construction (Black et al., 2004), etc.

[1]Department of Structural Engineering, University of California – San Diego, La Jolla, CA, USA
[2]State Key Lab of Automotive Safety and Energy, Tsinghua University, Beijing, China
[3]Department of Civil and Environmental Engineering, Michigan State University, East Lansing, MI, USA
[4]Program of Materials Science and Engineering, University of California – San Diego, La Jolla, CA, USA

Corresponding author:
Yueting Sun, State Key Lab of Automotive Safety and Energy, Tsinghua University, Beijing 100084, China.
Email: syt@tsinghua.edu.cn

Due to the high compressibility, thin-walled and cellular structures have come into widespread use, such as steel tubes and aluminum honeycombs (Gibson and Ashby, 1999; Meza et al., 2014). Cell wall buckling is their major energy absorption mechanism. One ''bottleneck'' is that the buckling initiation often requires a relatively high crush force, which lowers the energy absorption efficiency. A promising method to solve this problem is to introduce a filler, especially a liquid filler. With a high fluidity, a liquid filler can well fit with the cell walls.

However, most liquids are incompressible and cannot accommodate the cell-wall buckling. Recently, the authors of this paper carried out a set of experiments on nanoporous-materials-functionalized (NMF) liquid, which is composed of nanoporous materials and a liquid matrix (Han and Qiao, 2006; Sun et al., 2013, 2014a, 2014b, 2015; Surani et al., 2005). The nanopores are pre-treated to be hydrophobic; thus, the liquid stays outside of the nanopores. When a stress wave is applied and the wave pressure exceeds the critical infiltration pressure (P_{in}), the liquid can be intruded into the nanopores. Accompanied with the liquid infiltration, a certain amount of energy, $\alpha \cdot P \cdot V_p$ (Xu et al., 2014a), would be dissipated, with P being the wave pressure, V_p the nanopore volume, and $\alpha < 1$ a system parameter.

When a steel tube is filled by a NMF liquid, the quasi-static buckling mode can be fundamentally different from that of the empty tube (Chen et al., 2006). Preliminary experiments and finite element simulations on NMF liquid-filled tubes and microtruss structures showed that their energy absorption efficiency might be considerably improved (Liu et al., 2014; Sun et al., 2014c). While encouraging, these results are still non-conclusive because the loading conditions were quasi-static and the effects of the NMF liquid parameters, e.g. the infiltration pressure and the pore volume, are unclear. Hereby, an experimental investigation on NMF liquid-filled structures was performed under both quasi-static and dynamic loading conditions, and the NMF liquid parameters were varied in controlled ranges. The interaction between the NMF liquid and the tube wall was analyzed.

Experimental

Sample preparation

The testing sample, as shown in Figure 1, comprised a hollow stainless steel tube, two steel end-caps, and a NMF liquid that filled the steel tube. Such a configuration has been proven efficient for sealing

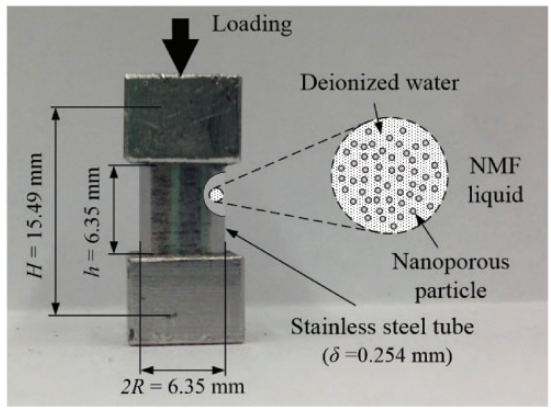

Figure 1. A testing sample of NMF liquid-filled steel tube.
NMF: nanoporous-materials-functionalized.

liquid components and it may also be directly relevant to future engineering applications (Chen et al., 2006). The height, outer diameter, and wall thickness of the stainless steel tube were $H = 15.49\,\text{mm}$, $2R = 6.35\,\text{mm}$, and $\delta = 0.254\,\text{mm}$, respectively. The tube was obtained from McMaster-Carr (Product No. 89895K719) and cut to length. The NMF liquid was sealed by firmly attaching the two end-caps with J-B Weld epoxy adhesives from both ends of the steel tube. On each end-cap, there was a matching hole with the depth of 4.57 mm, to enhance the sealing. No leakage could be observed at the sealing sections before and after all the experiments. In the assembled sample, the gauge length of the tube between the two end-caps was $h = 6.35\,\text{mm}$.

The NMF liquid in all the samples was based on deionized water, but involved two types of nanoporous materials to obtain different infiltration pressures. The first one was a Huber Zeoflo-TL macroporous silica. In order to increase the degree of hydrophobicity, the macroporous silica was surface treated by chlorotrimethylsilane in dry toluene. The chlorotrimethylsilane content was 20 vol.%, with 2 vol.% pyridine as the catalyst. The mixture of the silica and the treatment reagents was refluxed at 95°C for 72 h, after which the silica was filtered, thoroughly rinsed by ethyl alcohol, and dried in vacuum at 110°C for 12 h. The details of the surface treatment procedure were discussed in Han et al. (2007; 2009). The specific pore volume of the macroporous silica was around $1.7\,\text{cm}^3/\text{g}$; the average pore size was around 100 nm; and the average particle size was 4 μm. The second nanoporous material was a Fluka 100-C_8 mesoporous silica, with an average nanopore size of 7.8 nm. The specific surface area was $287\,\text{m}^2/\text{g}$ and the specific pore volume was $0.55\,\text{cm}^3/\text{g}$, characterized by a Micromeritics ASAP-2000 Gas Adsorption Analyzer. The particle size ranged from 15 to 35 μm.

The infiltration pressures of the two types of nanoporous silicas were characterized through quasi-static pressure-induced infiltration tests. In a thick-walled stainless steel cylinder, two steel pistons equipped by reinforced gaskets sealed about 0.2 g of nanoporous silica particles and 6.0 g of deionized water. By using a type-5582 Instron machine, the upper piston was compressed into the cylinder at a constant rate of 5 mm/min. Details of the experimental setup have been described elsewhere (Qiao et al., 2006). Figure 2 shows typical sorption isotherm curves. The pressure P in liquid phase was calculated as the piston force divided by the piston cross-sectional area; the specific volume ΔV was estimated as the piston displacement multiplied by the piston cross-sectional area, normalized by the silica mass. The infiltration pressures of Zeoflo-TL and Fluka 100-C_8 were

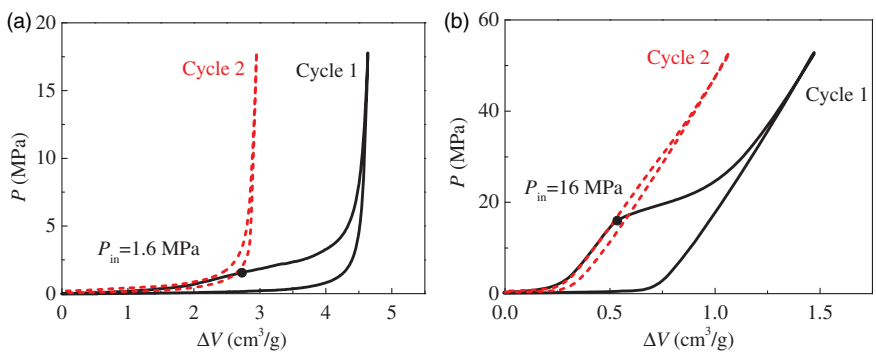

Figure 2. Typical P-ΔV curves of (a) Zeoflo-TL silica and (b) Fluka 100-C_8 silica.

Table 1. The list of testing samples.

Parameters	H	Z1	Z2	F
Nanoporous material	–	Zeoflo-TL	Zeoflo-TL	Fluka 100-C_8
Mass of nanoporous material (mg)	–	26	80	80
Pore volume (mm^3)	–	44	136	44
Infiltration pressure (MPa)	–	1.6	1.6	16

measured to be 1.6 and 16 MPa, respectively. After the applied pressure reached a relatively high level (18 and 53 MPa for these two silicas, respectively), the crosshead of the loading machine moved back, until the piston pressure vanished. The same loading–unloading cycle was repeated for multiple times. The P-ΔV curves at the first and the second loadings were different; while from the second loading, the system performance converged to a steady state. Therefore, in Figure 2, only the first two loading cycles are shown.

Table 1 lists the four types of assembled steel-tube samples. Sample H was the reference hollow tube. Samples Z1 and Z2 were based on Zeoflo-TL but contained different amounts of silica, so that they had the same infiltration pressure but different pore volumes. Sample F was based on Fluka 100-C_8, so that it had a much higher infiltration pressure but its pore volume equaled to that of sample Z1. In this arrangement, the influence of infiltration pressure and pore volume could be analyzed separately.

Testing methods

The sealed, end-capped tube samples were analyzed through a series of quasi-static compression, drop weight impact, and Split Hopkinson Bar (SHB) experiments. Quasi-static compression tests were conducted by the type-5582 Instron machine. The samples were crushed from the top, with a constant loading rate of 5 mm/min. A slower loading rate did not lead to any variations in sample behaviors. The relationship between the nominal stress $\sigma = F/(\pi R^2)$, and the nominal strain $\varepsilon = d/h$ was analyzed, where F is the compression force and d is the crosshead displacement.

Drop weight tests were carried out by an Instron CEAST 9350 drop tower shown in Figure 3. The tube sample was placed at the top center of the base, and the drop hammer was lifted along the guide rail to the designated height. In this test, the impact mass was set to 2.77 kg and the drop height was 0.63 m; this provided a dynamic impact loading of 3.5 m/s, corresponding to an effective strain rate of 471 s^{-1}. As the test started, the drop hammer fell freely and impacted on the tube sample. By the accelerometer amounted on the drop hammer, the acceleration data was collected during the impact process, from which the compression force and displacement were computed.

Higher rate impact responses of the tube samples were characterized by a SHB system. As depicted in Figure 4, a stainless steel striker was projected by a high-pressure gas chamber and impacted on a stainless steel incident bar at 12.3 m/s, corresponding to a strain rate of 1937 s^{-1}. The testing sample was sandwiched between the incident bar and a stainless steel transmitted bar. The lengths of the striker, the incident bar, and the transmission bar were 457.2, 1778, and 1524 mm, respectively, and their diameters were all 12.7 mm. The testing condition was maintained the same for all the samples. Profiles of incident and reflected waves were measured from the incident bar by a Vishay WK-13-250BF-10 C strain gauge, equipped with a Vishay 2310B data acquisition system. Profiles of transmitted waves were measured from the transmitted bar.

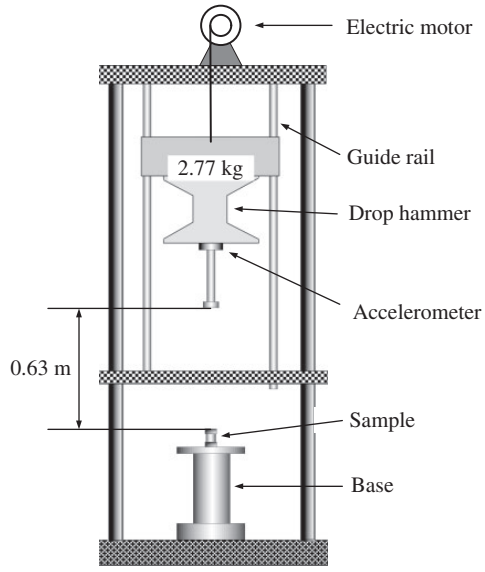

Figure 3. Schematic of the drop weight testing setup.

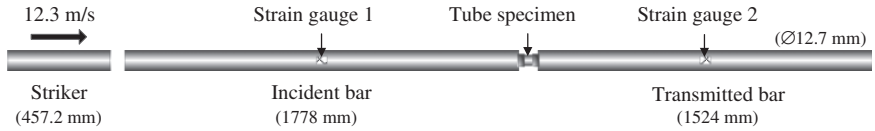

Figure 4. Schematic of the SHB testing setup.

Results and discussion

Quasi-static behavior

Figure 5 shows the typical stress–strain curves and buckling modes of the tube samples. The reference tube sample H undergoes a regular buckling process, forming a stress at about 36 MPa in the stress–strain curve. The initiation pressure of buckling is 72 MPa, much higher than the pressure of the buckling plateau, as the wrinkle formation in a straight tube wall is more difficult than the wrinkle propagation.

When the tube is filled with NMF liquid, its initial linear compression section and the onset of buckling are quite similar with that of the hollow tube. During the buckling initiation, the lateral expansion of the tube wall at its two ends, which corresponds to the high initiation pressure of buckling, prevents the tube volume from decreasing, as shown in Figure 6. Consequently, inner pressure is quite small. That is, the liquid filler inside does not affect the buckling initiation, so the NMF liquid-filled tube samples (Z1, Z2, and F) have nearly identical configurations and stress levels with the hollow sample H. In comparison, a solid filler tends to increase the initiation pressure of buckling because of its ability to resist shear stresses.

Once the buckling begins, the tube volume shrinks and the NMF liquid filler carries a considerable inner pressure, so that the tube responds differently from hollow tubes. As the liquid pressure

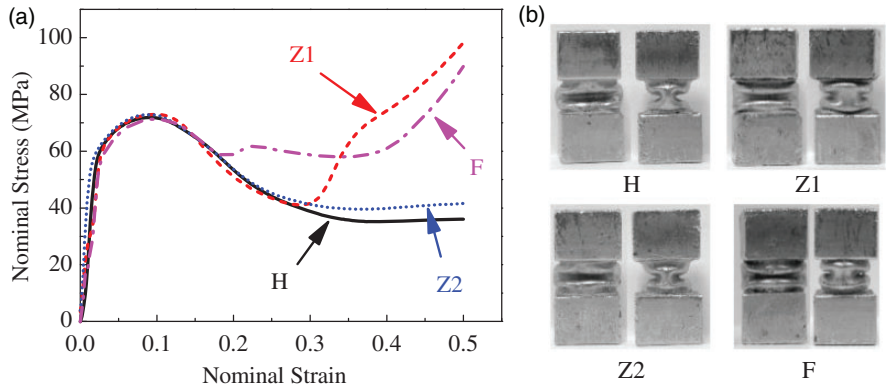

Figure 5. Typical quasi-static testing results: (a) nominal stress-strain curves, (b) typical configurations of buckled tube samples: front view (left) and side view (right).

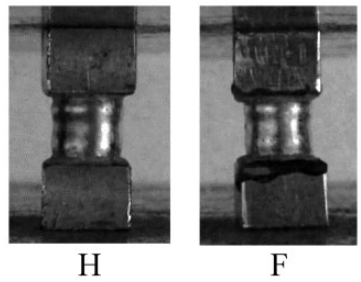

Figure 6. Comparison of tube configurations with and without NMF liquid filler during buckling initiation.

reaches P_{in}, water molecules infiltrate into the nanopores, and the volume of the liquid filler reduces under a nearly constant pressure, resulting in a high post-buckling plateau. Once all nanopores are filled, the liquid filler becomes incompressible again, causing a sharply increased crush pressure.

Clearly, both infiltration pressure and pore volume have significant impacts on the crush behaviors of NMF liquid-filled tubes, evidenced by Figure 5. The comparison between samples Z1 and Z2 shows the influence of pore volume. With a sufficient pore volume, the liquid infiltration in sample Z2 continues even at the late stage of tube wall buckling; the pore volume of sample Z1 is consumed rapidly when compression strain is only ~0.3. The pore volume determines the compressibility of the NMF liquid.

The infiltration pressure influences the crush pressure of the post-buckling plateau. The buckling plateaus of samples Z1 and Z2 are slightly higher than that of the hollow tube, as infiltration pressure is only ~1.6 MPa; while sample F has a much higher plateau since its infiltration pressure is ~16 MPa, higher by an order of magnitude.

As shown in Figure 5(b), the shapes of the buckling patterns of all the samples are similar. The distinct detailed features come from the difference in inner pressure. Lateral plastic yielding of tube wall is pronounced in samples Z1 and F, where the inner pressure is high; and least evident in samples H and Z2, where the inner pressure is much lower. Higher inner pressure may come from

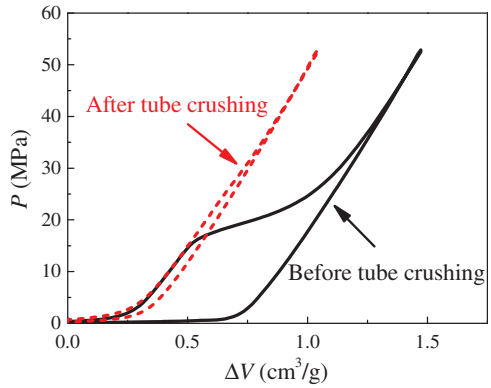

Figure 7. Typical P-ΔV curves of NMF liquid in sample F before and after compression.

higher infiltration pressure or insufficient pore volume, while lower inner pressure requires a low infiltration pressure with sufficient pore volume.

In order to validate that water molecules have indeed enter the nanopores during the tube compression, the nanoporous particles are taken out of the tubes after the compression experiment, and infiltration tests are conducted again, through a similar procedure as in "Experimental" section. Figure 7 shows that even for sample F with the highest infiltration pressure, the tube crushing has activated the liquid infiltration and all the nanopores have been filled up. No infiltration plateau can be observed in the subsequent infiltration tests.

The quasi-static crush behaviors indicate that the NMF liquid filler mainly influences the post-buckling stage, wherein the crush pressure increases with the infiltration pressure and the tube compressibility increases with the pore volume. It is well known that the infiltration pressure can be adjusted by changing the pore size or the solid/liquid interfacial tension, and the pore volume can be modified by controlling the mass ratio of nanoporous material (Qiao et al., 2009; Sun et al., 2015). Therefore, the NMF liquid-filled tube can offer a high crush force and an excellent compressibility at the same time (Baumeister et al., 1997).

Dynamic behavior

Figure 8 shows the low-rate impact response. The influence of the infiltration pressure and the pore volume is similar as that of quasi-static tests. The NMF liquid filler enhances the tube post-buckling, with its crush pressure and compressibility depending on the infiltration pressure and pore volume, respectively. Sample F has a high crush pressure due to its high infiltration pressure, and the post-buckling plateaus of samples Z1 and Z2 are close to that of the hollow sample H with their low infiltration pressure. Samples F and Z1 have limited compressibility, compared with sample Z2 which has sufficiently high pore volume. However, under dynamic impact, the crush pressures are higher than that of quasi-static tests. For instance, the initiation pressure buckling of sample H reaches around 100 MPa, higher than the quasi-static value by nearly 40%.

In the SHB experiment, the sample is subjected to the dynamic loading generated through the impact of the striker on the incident bar. The stress wave propagates across the incident bar, and with a certain reflection, a part of the stress wave goes through the testing sample and enters into the transmitted bar. Figure 9 shows the typical transmitted stress waves, reflecting the stresses on the back end of the specimen. In the first 0.15 ms, there is no statistically meaningful difference among

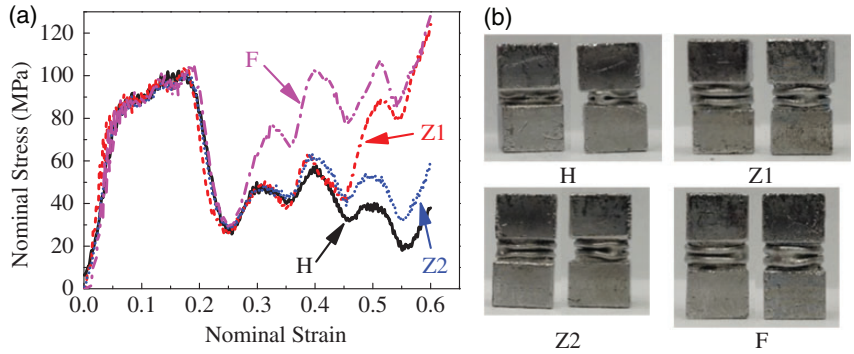

Figure 8. Typical drop weight testing results: (a) nominal stress–strain curves, (b) typical configurations of buckled tube samples: front view (left) and side view (right).

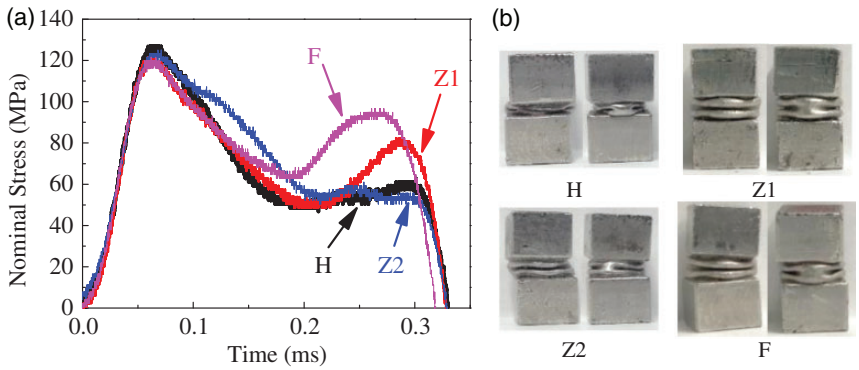

Figure 9. Typical SHB testing results: (a) transmitted pulses, (b) typical configurations of buckled tube samples: front view (left) and side view (right).

all the samples, as they should be, since the pulse front is governed by the wave propagation along the steel tube wall. As the tube volume decreases, the transmitted waves become different. For sample Z2, with a low infiltration pressure and a large pore volume, the pressure of the transmitted wave rapidly decreases from about 120 MPa to nearly 60 MPa, similar to the hollow sample H. The transmitted waves of samples Z1 and F first decrease, due to the infiltration mechanism, and then increase, when the nanopores are filled.

It is clear that the liquid infiltration mechanism works well under the dynamic condition and enhances the post-buckling performance. The buckling modes are somewhat insensitive to the loading rate; the rate effect is more evident on the crush force.

Crush performance analysis

The areas under the stress–strain curves in Figures 5 and 8 reflect the energy absorption $\Delta U = \int_0^{\varepsilon_D} V_0 \sigma d\varepsilon$, where V_0 is the original volume; ε_D is the effective strain, which is taken as 0.5. For the SHB test (Figure 9), the wave energy $U = \xi \int_0^T \sigma^2 dt$, where T is the pulse duration and the system parameter $\xi = cA/(2E) + \rho A c^3/(2E^2) = 3.24 \times 10^{-12}\,\mathrm{m^5/N\,s}$ (Surani et al., 2005), with the

sound speed $c = 5.04 \times 10^3$ m/s; the Young's modulus $E = 1.97 \times 10^{11}$ Pa; the cross-sectional area $A = 126.68 \times 10^{-6}$ m^2; and the mass density $\rho = 7.75 \times 10^3$ kg/m^3. Thus, the energy absorption of the tube sample $\Delta U = U_I$-U_R-U_T, where U_I is the incident energy; U_R is the reflected energy; and U_T is the transmitted energy.

Table 2 shows the calculated energy absorption density under the three loading conditions. At each loading rate, the hollow sample H has the lowest energy absorption density. With the NMF liquid filler, the energy absorption density is considerably enhanced, primarily because the NMF liquid filler can absorb a relatively large amount of energy through liquid infiltration (Chen et al., 2008; Han et al., 2008; Xu et al., 2014a, 2014b) and also promotes the lateral plastic expansion of tube wall. Since a higher infiltration pressure is beneficial to both these two effects, sample F turns out to obtain the highest energy absorption density, and sample Z2 has a low energy absorption density, only slightly higher than that of the hollow tube H. However, sample Z1 has a relatively high energy absorption density despite of its low infiltration pressure, which is caused by the rapid rise of crush pressure as a result of its insufficient pore volume. But this is not a favorable way to enhance energy absorption due to the risk of tube wall failure and leakage.

Crush force efficiency (CFE) is an important factor of EAM, defined as the ratio of average force to peak force during the loading procedure. It reflects the ability of the crush force to remain constant. Its theoretical upper limit is 1, at which the highest possible energy absorption capacity is achieved. Table 3 lists the CFE of the tube samples under quasi-static condition. Samples Z2 and F have the highest CFE, while sample Z1 has the lowest. Due to low infiltration pressure and the large pore volume, sample Z2 reaches its peak crush pressure (~73 MPa) at the buckling initiation, similar to that of the hollow sample H (~72 MPa); while its average crush pressure (~51 MPa) is slightly higher than that of sample H (~48 MPa). Samples F and Z1 have relatively low nanopore volumes, so that their peak crush pressures are reached at the maximum compressive strain. Sample F ends with a relatively lower peak crush pressure and a similar average crush pressure as sample Z1.

Table 2. Energy absorption density of tube samples under various loading conditions (J/cm^3).

Loading conditions	H	Z1	Z2	F
Quasi-static	23.98	31.24	25.42	31.39
Drop weight impact	28.56	30.25	29.50	36.97
SHB impact	13.93	28.86	17.71	33.73

Table 3. Performance of NMF liquid-filled tubes under quasi-static condition.

Evaluations	H	Z1	Z2	F
Energy absorption (J)	4.82	6.28	5.11	6.31
Peak crush pressure (MPa)	71.92	98.26	73.00	89.93
Average crush pressure (MPa)	48.00	62.48	50.88	62.81
Crush force efficiency	0.67	0.64	0.70	0.70

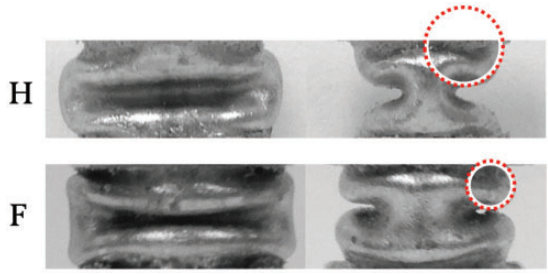

Figure 10. Comparison of buckling modes of samples H and F, with the quasi-static compressive strain of 0.5.

Among all the samples under investigation, sample F has the highest energy absorption density and CFE, which should be attributed to its high infiltration pressure and the moderate peak force. In general, for a NMF liquid-filled tube, a large pore volume should be provided to ensure that the compressibility is sufficient; an appropriate infiltration pressure needs to be selected to reach the highest possible CFE. This can be regarded as a general rule to design NMF liquid-filled tubes, so as to enhance energy absorption density as well as CFE of tube structures.

The crushing of NMF liquid-filled tube involves the interaction between the tube wall and the liquid filler. The volume change of NMF liquid is dominated by the buckling mode of tube wall, while the NMF liquid pressure in turn affects the tube wall expansion and buckling. Figure 10 shows the influence of NMF liquid pressure on the buckling modes of samples H and F. They exhibit different wrinkles. For hollow sample with no inner pressure, the tube wall can deform either inward or outward, while with the pressurized liquid phase, the intrusion of tube wall is difficult. Thus, sample H has two half wrinkles at fixed ends, and sample F has smaller complete wrinkles, i.e. higher order buckling modes are triggered, somewhat similar to aluminum foams with solid fillers (Hanssen et al., 2001). The interaction between the tube wall and the liquid filler also affects the crush force and the energy absorption. Generally, a higher order buckling mode leads to a higher crush pressure and more energy dissipation of tube wall. For the NMF liquid, its energy dissipation depends on both the inner pressure and the volume variation, associated with buckling configuration.

Conclusions

In summary, the crush behavior of NMF liquid-filled steel tubes is experimentally investigated under various loading conditions. The NMF liquid filler mainly influences the tube behaviors by increasing the crush force, changing the buckling mode, and enhancing the energy absorption capacity, not only through the liquid infiltration but also through the plastic deformation of tube wall. The crush force and the compressibility can be independently adjusted by the infiltration pressure and the pore volume, respectively. A general design method of NMF liquid-filled tube is proposed to enhance the energy absorption and crush force efficiency simultaneously. The interaction between the tube wall and the liquid filler depends on their material properties, critical to the buckling mode and the crush force. These findings will help understand the mechanical behavior of NMF liquid-filled structures and promote their applications in engineering practice.

Declaration of Conflicting Interests

The author(s) declared no potential conflicts of interest with respect to the research, authorship, and/or publication of this article.

Funding

The author(s) disclosed receipt of the following financial support for the research, authorship, and/or publication of this article: Four of the authors (CZ, MW, WL, and YQ) gratefully acknowledge the support from the Army Research Office under Grant No. W911NF-12-1-0011. Two of the authors (YS and YL) are supported by the Tsinghua University under Grant No. 20121080050 and the National Natural Science Foundation of China under Grant No. 11372164.

References

Baumeister J, Banhart J and Weber M (1997) Aluminium foams for transport industry. *Materials & Design* 18: 217–220.

Black CJ, Makris N and Aiken ID (2004) Component testing, seismic evaluation and characterization of buckling-restrained braces. *Journal of Structural Engineering* 130: 880–894.

Chen X, Cao G, Han A, et al. (2008) Nanoscale fluid transport: Size and rate effects. *Nano letters* 8: 2988–2992.

Chen X, Surani FB, Kong X, et al. (2006) Energy absorption performance of steel tubes enhanced by a nanoporous material functionalized liquid. *Applied Physics Letters* 89: 241918.

Gibson LJ and Ashby MF (1999) *Cellular Solids: Structure and Properties*. Cambridge: Cambridge University Press.

Han A, Lu W, Punyamurtula VK, et al. (2008) Effective viscosity of glycerin in a nanoporous silica gel. *Journal of Applied Physics* 104: 124908.

Han A, Lu W, Punyamurtula VK, et al. (2009) Temperature variation in liquid infiltration and defiltration in a MCM41. *Journal of Applied Physics* 105: 024309.

Han A and Qiao Y (2006) Pressure-induced infiltration of aqueous solutions of multiple promoters in a nanoporous silica. *Journal of the American Chemical Society* 128: 10348–10349.

Han A and Qiao Y (2007) Controlling infiltration pressure of a nanoporous silica gel via surface treatment. *Chemistry Letters* 36: 882–883.

Hanssen A, Langseth M and Hopperstad O (2001) Optimum design for energy absorption of square aluminium columns with aluminium foam filler. *International Journal of Mechanical Sciences* 43: 153–176.

Liu Y, Schaedler TA, Jacobsen AJ, et al. (2014) Quasi-static crush behavior of hollow microtruss filled with NMF liquid. *Composite Structures* 115: 29–40.

Lu G and Yu T (2003) *Energy Absorption of Structures and Materials*. Boca Raton, FL: CRC Press.

Majumdar A, Butola BS and Srivastava A (2013) Optimal designing of soft body armour materials using shear thickening fluid. *Materials & Design* 2013; 46: 191–198.

Meza LR, Das S and Greer JR (2014) Strong, lightweight, and recoverable three-dimensional ceramic nanolattices. *Science* 2014; 345: 1322–1326.

Qiao Y, Punyamurtula VK, Han A, et al. (2006) Temperature dependence of working pressure of a nanoporous liquid spring. *Applied Physics Letters* 89: 251905.

Qiao Y, Liu L and Chen X (2009) Pressurized liquid in nanopores: A modified Laplace-Young equation. *Nano letters* 9: 984–988.

Sun Y, Xu J, Li YB, et al. (2013) Experimental study on energy dissipation characteristics of ZSM – 5 zeolite/water system. *Advanced Engineering Materials* 15: 740–746.

Sun Y, Li P, Qiao Y, et al. (2014a) Time-dependent gas-liquid interaction in molecular-sized nanopores. *Scientific Reports* 4: 6547.

Sun Y, Lu W and Li Y (2014b) A defiltration control method of pressurized liquid in zeolite ZSM-5 by silanol introduction. *Applied Physics Letters* 105: 121609.

Sun Y, Xu J, Zhao C, et al. (2014c) Exploring a new candidate of energy absorber: Thin-walled tube structures filled with nanoporous material functionalized liquid. *IRCOBI Conference* 66: 578–586.

Sun Y, Guo Z, Xu J, et al. (2015) A candidate of mechanical energy mitigation system: Dynamic and quasi-static behaviors and mechanisms of zeolite β/water system. *Materials & Design* 66: 545–551.

Surani FB, Kong X, Panchal DB, et al. (2005) Energy absorption of a nanoporous system subjected to dynamic loadings. *Applied Physics Letters* 87: 163111.

Xu B, Chen X, Lu W, et al. (2014a) Non-dissipative energy capture of confined liquid in nanopores. *Applied Physics Letters* 104: 203107.

Xu B, Qiao Y and Chen X (2014b) Mitigating impact/blast energy via a novel nanofluidic energy capture mechanism. *Journal of the Mechanics and Physics of Solids* 62: 194–208.

Zhang Y, Sun G, Li G, et al. (2012) Optimization of foam-filled bitubal structures for crashworthiness criteria. *Materials & Design* 38: 99–109.